Multiple metamagnetic transitions induced by high magnetic field in DyBi

Jun Zhao,[1,2,3,*] Azizur Rahman,[2,1,*] Wei Liu,[4] Fanying Meng,[1,2,3] Langsheng Ling,[1,3] Yuyan Han,[1,3] Chuanying Xi,[1,3] Wei Tong,[1,3] Longmeng Xu,[5] Zhaoming Tian,[5,†] Li Pi,[1,2,3] Lei Zhang,[1,3,‡] and Yuheng Zhang[1,2,3]

[1]*Anhui Key Laboratory of Condensed Matter Physics at Extreme Conditions, High Magnetic Field Laboratory, Hefei Institutes of Physical Science, Chinese Academy of Sciences, Hefei 230031, China*

[2]*Department of Physics, University of Science and Technology of China, Hefei 230026, China*

[3]*The High Magnetic Field Laboratory of Anhui Province, Hefei 230031, China*

[4]*Institutes of Physical Science and Information Technology, Anhui University, Hefei, 230601, China*

[5]*Wuhan National High Magnetic Field Center and School of Physics, Huazhong University of Science and Technology, Wuhan 430074, China*

(Received 26 July 2022; revised 23 November 2022; accepted 2 December 2022; published 16 December 2022)

The rare-earth monopnictide compounds have recently received considerable attention in condensed matter physics because of their correlation between magnetism, crystallographic structure, and transport. Here, we report experimental observations of high-magnetic-field-induced multiple metamagnetic transitions and magnetic structures in DyBi single crystals. The external field up to 32 T is applied in three distinct crystallographic directions as $H//[001]$, $H//[011]$, and $H//[111]$, which reveals anisotropic magnetism as well as multiple metamagnetic transitions. Two field-induced magnetic phase transitions at 3.7 T and 4.9 T along $H//[001]$, two at 3.8 T and 24 T along $H//[011]$, and one at 3.8 T along $H//[111]$ are identified. In order to unveil the nature of magnetic interaction in DyBi, the critical behavior analysis for $H//[001]$, a direction with typical magnetism and transitions, is performed. The yielded critical exponents $\beta = 0.234(8)$, $\gamma = 0.904(3)$, and $\delta = 5.03(2)$ agree well with the theoretical prediction of a tricritical mean-field model, indicating a field-induced tricritical phenomenon in this system. Comprehensive magnetic phase diagrams for $H//[001]$, $H//[011]$, and $H//[111]$ are constructed based on detailed magnetization measurement and scaling, which reveal multiple phases such as NiO-type antiferromagnetic (AFM), HoP-type AFM, forced ferromagnetic (FFM), and paramagnetic (PM) phases. Two tricritical points (TCPs) are determined at the intersections of the AFM, FFM, and PM phases, with TCP = (8.6 K, 85 kOe) for $H//[001]$ and (16.8 K, 243 kOe) for $H//[011]$. The recognition of multiple phases suggests delicate and complex competition and balance between variable couplings in this system.

DOI: 10.1103/PhysRevB.106.224412

I. INTRODUCTION

Since the discovery of an unprecedentedly large magnetoresistance (MR) in LaSb, there has been a surge of interest in rare-earth monopnictides *RPn* (R = rare earth, Pn = Sb, Bi). For its heavy-fermion nature, the family was extensively researched in the 1980s and 1990s [1]. Recently, *RPn* has been demonstrated to exhibit extremely large MR, suggesting that it could be used in spintronics devices, magnetic memory, and magnetic field sensors [2–7]. *RPn* has similar magnetotransport properties to topological nontrivial semimetals like WTe_2 [8], Cd_3As_2 [9,10], TaAs [11], and NbP [12]. Therefore, this class of materials may host topologically nontrivial phases. Following that, extensive studies on this family were conducted systematically [2–7]. Intriguingly, recent theoretical research suggests that La*Pn* (Pn = N, P, As, Sb, and Bi) could be a topological prototype with band inversion at the X point of the bulk fcc Brillouin zone [13]. For example, angle-resolved photoelectron spectroscopy (ARPES) and first-principles calculations show that LaBi has topologically nontrivial surface states [14]. The existence of a nontrivial Z_2 invariant in YBi indicates that it could be a topological semimetal candidate [15]. The discovery of antiferromagnetic (AFM) ordering in *R*Sb (R = Ce, Nd, Gd-Er) at low temperatures [5,7,16,17] and ferromagnetic (FM) ordering in CeBi has further enriched the properties of *RPn*. As a result of the simultaneous existence of intrinsic magnetism and topology, *RPn* has received a lot of attention as a new platform for studying the interactions between chirality, magnetism, correlation, and topological order, which opens up new possibilities for novel quantum states, spin-polarized chiral transport, and exotic optical phenomena [18].

DyBi, another member of the rare-earth monopnictide family, has a rocksalt-type structure at room temperature [Fig. 1(a)], namely cubic symmetry with space group $Fm\bar{3}m$ [19]. Earlier research revealed that DyBi undergoes a first-order phase transition to the AFM state with tetragonal structure at the Néel temperature (T_N = 11.2 K), and both the tetragonal and cubic reflections are present within a 0.05 K range around T_N [19,20]. Aside from the magnetostructural transition in DyBi, the field dependence of magnetization is

*These authors contributed equally to this work.
†Corresponding author: tianzhaoming@hust.edu.cn
‡Corresponding author: zhanglei@hmfl.ac.cn

 ©2022 American Physical Society

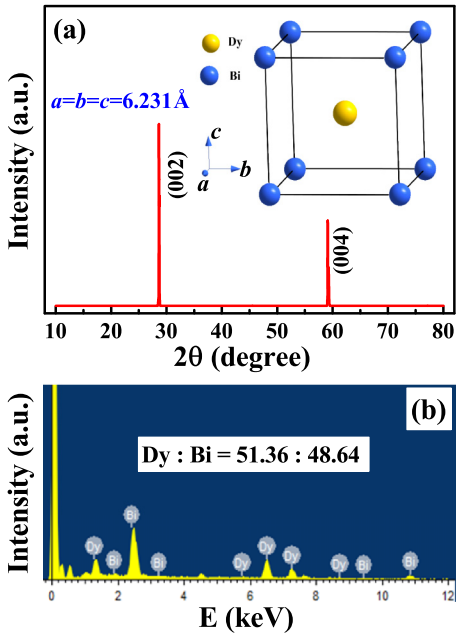

FIG. 1. (a) XRD pattern for single-crystal DyBi (inset shows crystal structure of DyBi). (b) Typical EDX spectrum for DyBi.

also elusive [19]. The magnetization along [001] abruptly switches to one half of its saturation value at an intermediate field strength (the ground-state level of the molecular field-split Kramers doublet $F6$ has a magnetic moment of 9.9 μ_B). This spin flip occurs at slightly lower fields along [110] and [111]. At 1.5 K, with a magnetic field applied along [001], DyBi completely polarizes into an FM state at 52 kOe, whereas the very large anisotropy energy prevents an FM orientation along [110] and [111], and indeed, no sign of a second transition was found up to 200 kOe [19]. As a result, the magnetic structure along [001] is more complicated than those along [110] and [111]. Therefore, DyBi offers a platform for studying the directional-dependent magnetic phase diagrams and intricate magnetic interactions.

Here, we aim at the exotic metamagnetic transitions in the DyBi single crystal by employing the universality principle to identify the magnetic mechanism and properties. As the field up to 32 T is applied along variable crystal directions, multiple metamagnetic transitions and magnetic orderings, some of which have not been previously reported, are induced. The critical behavior analysis indicates a tricritical phenomenon with multiple phases. The H-T phase diagrams for variable crystal directions are constructed, which unveil multiple magnetic structures such as the NiO-type AFM ground state, the field-modulated HoP-type AFM, and the polarized FM phases.

II. EXPERIMENTAL METHODS

The self-flux technique was used to grow DyBi single crystals. Under an argon atmosphere, high-purity powders of Dy (99.9%) and Bi (99.999%) were mixed in a mole ratio of 1 : 10 and sealed into a quartz tube. The sealed quartz tube was heated to 1150 °C, then slowly cooled to 700 °C. Finally, the extra Bi flux was removed by centrifugation to yield DyBi single crystals.

The structure and crystal orientations were determined by x-ray diffraction (XRD) (Rigaku-TTR3 x-ray diffractometer) with Cu K_α radiation. An energy-dispersive x-ray spectrometer (EDXS) was used to examine the chemical compositions. The angle, temperature, and field dependence of magnetization were measured by a Quantum Design vibrating sample magnetometer (SQUID-VSM). To obtain the initial isothermal magnetization, the sample was heated to room temperature and held for 2 minutes before being cooled to the target temperature under zero field. To ensure a precise magnetic field before data acquisition, a no-overshoot mode was used, and the magnetic field was relaxed using an oscillation model. Magnetization under high magnetic field was carried out on a water-cooling resistive magnet.

III. RESULTS AND DISCUSSION

Figure 1(a) depicts the XRD pattern of single-crystal DyBi, where only $(00l)$ peaks were observed. A set of sharp diffraction peaks demonstrates high crystalline quality of the as-grown single crystal. The inset of Fig. 1(a) shows a structural schematic diagram of DyBi, which crystallizes as a NaCl-type cubic structure with the space group $Fm\bar{3}m$ [21]. Based on the XRD pattern, the lattice constants are calculated as $a = b = c = 6.231$ Å consistent with the previous report [22]. The chemical ratio of a well-polished single crystal is determined by EDX spectroscopy, which is performed at various positions on the crystal surfaces. The typical EDX spectrum in Fig. 1(b) reveals chemical proportions Dy : Bi = 51.36 : 48.64, the stoichiometry of which is within the experimental errors [19,23].

Figures 2(a)–2(c) depict the temperature-dependent magnetization $[M(T)]$ under zero-field-cooled (ZFC) and field-cooled (FC) sequences with $H = 200$ Oe along the [001] ($H//[001]$), [011] ($H//[011]$), and [111] ($H//[111]$) directions. Each $M(T)$ curve has a cusp corresponding to a magnetic phase transition. Above the phase transition, M increases as temperature decreases, exhibiting a paramagnetic (PM) behavior. The temperature-dependent reciprocal of susceptibility $[\chi(T)]$ curves are plotted on the right axis in Figs. 2(a)–2(c), the linear feature of which confirms the PM phase at higher temperature. The Curie-Weiss law $[\chi(T) = C/(T - \Theta_{CW})]$ fittings of $\chi^{-1}(T)$ give $\Theta_{CW} = -7.31$ K for $H//[001]$, $\Theta_{CW} = -10.91$ K for $H//[011]$, and $\Theta_{CW} = -6.21$ K for $H//[111]$. The negative values of Θ_{CW} imply an AFM coupling in DyBi. Below the phase transition temperature, ZFC and FC $M(T)$ curves superimpose exactly regardless of field orientations, demonstrating an AFM ground state. The AFM transition temperature (T_N) can be determined by the peak as $T_N \sim 11.5$ K. Figures 2(d)–2(f) show $M(T)$ curves under selected fields for $H//[001]$, $H//[011]$, and $H//[111]$, respectively, with insets enlarging the phase transition areas. Under lower fields, $M(T)$ curves exhibit PM-AFM phase transitions in all three crystal directions. The PM-AFM phase transitions under lower field, however, are modulated by the external field into PM-FM phase transitions under higher field. Below $H = 2$ T, $M(T)$ curves exhibit thermal hysteresis, as shown in the insets of Figs. 2(d)–2(f),

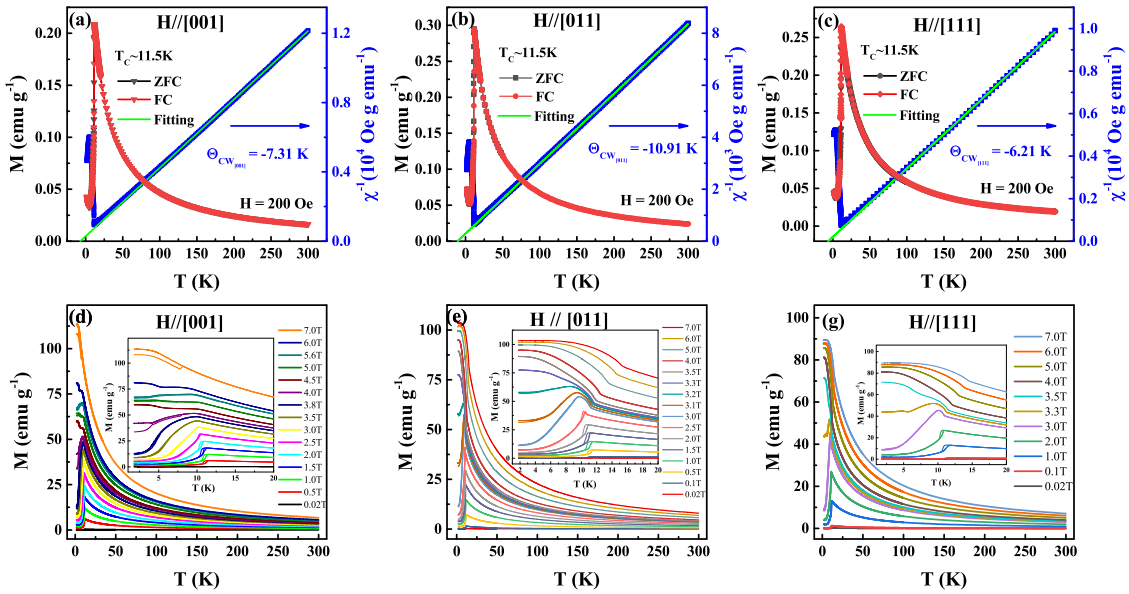

FIG. 2. Temperature-dependent magnetization $[M(T)]$ and reciprocal susceptibility $[\chi^{-1}(T)]$ under $H = 200$ Oe with (a) $H//[001]$, (b) $H//[011]$, and (c) $H//[111]$. $M(T)$ curves under selected fields for (d) $H//[001]$, (e) $H//[011]$, and (f) $H//[111]$ [inset magnifies $M(T)$ in the low-temperature region].

which is typically associated with a first-order phase transition. This first-order phase transition has been previously reported, where the cubic unit cell transforms abruptly into a monoclinic one at this temperature [19]. An analogous phenomenon has also been observed in isostructural DySb [24].

Figure 3(a) depicts the field dependence of isothermal magnetization $[M(H)]$ at $T = 1.8$ K with applied fields up to 32 T along $H//[001]$, $H//[011]$, and $H//[111]$, respectively. The $M(H)$ curve for $H//[001]$ exhibits a saturation behavior after two steps at 3.7 T and 4.9 T, corresponding to three field-induced magnetic phase transitions,

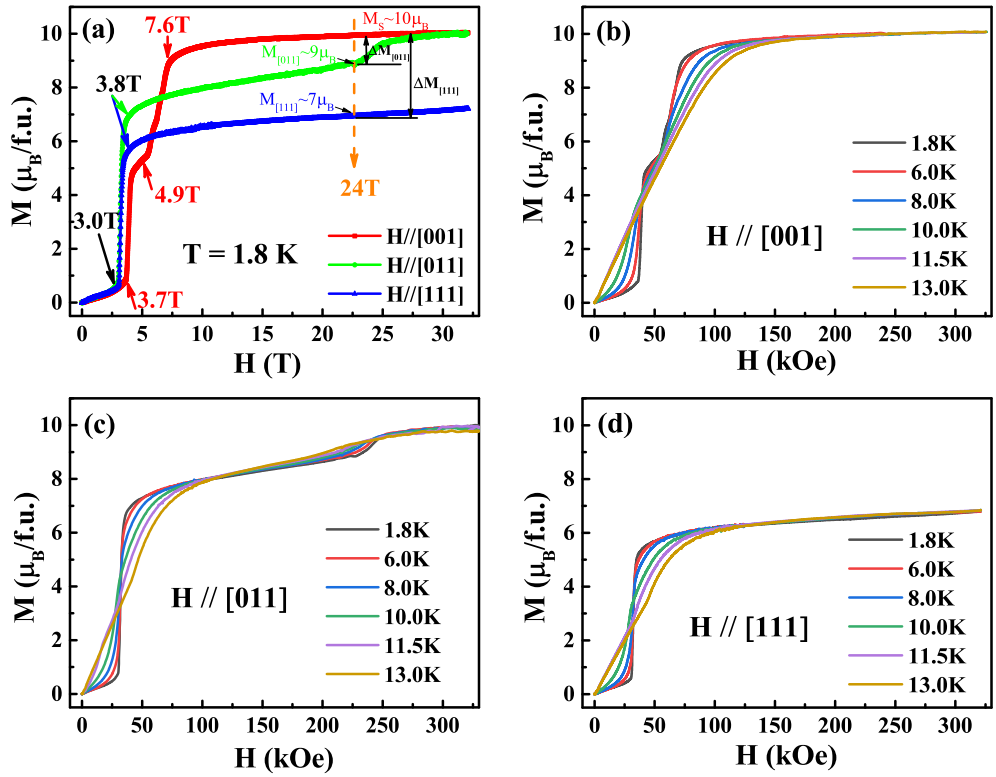

FIG. 3. (a) Field dependence of isothermal magnetization $[M(H)]$ at $T = 1.8$ K up to 32 T with $H//[001]$, $H//[011]$, and $H//[111]$ directions. (b), (c), and (d): $M(H)$ curves for $H//[001]$, $H//[011]$, and $H//[111]$ at selected temperatures.

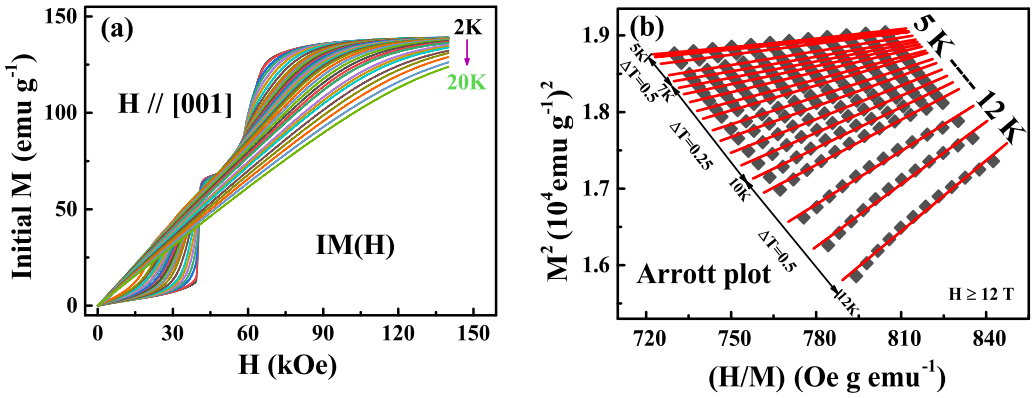

FIG. 4. (a) Field dependence of initial magnetization [IM(H)] with $H//[001]$. (b) Arrott plot of M^2 vs H/M.

respectively. The saturation magnetization M_S approximates $M_S \sim 9.9\ \mu_B$/f.u. above 7.6 T, which approaches the theoretical value 9.95 μ_B/f.u. of Dy^{3+} [19]. It is noted that the second step approximately corresponds to one half of M_S. For $H//[011]$, the $M(H)$ curve exhibits two steps located at 3.0 T and 24 T, respectively. When H exceeds 24 T, the magnetization also displays a saturation behavior to M_S. This demonstrates that as the magnetic field increases, the modulated magnetic state first transforms into an intermediate phase before polarizing into an FM phase for $H//[011]$. However, for $H//[111]$, there is only one step at 3.0 T. Although $M(H)$ for $H//[111]$ also exhibits a saturation behavior, the saturation magnetization is only $\sim$7.2 μ_B/f.u. In other words, the FM phase is still not realized until 32 T for $H//[111]$. Figures 3(b)–3(d) show the $M(H)$ steps at selected temperatures. As temperature increases, the steps become less obvious, and then finally disappear above T_N. The distinct behaviors in three directions indicate anisotropic magnetism and field-induced rich magnetic phases in DyBi. The magnetic behaviors, critical temperature T_C, and saturation magnetization M_S are highly consistent with previous reports, confirming the high quality of the sample used [19,23].

In order to clarify the nature and classification of magnetic interaction, an in-depth critical behavior investigation is carried out for $H//[001]$, a direction with typical magnetism and transitions. Figure 4(a) shows the field-dependent initial magnetization [IM(H)] curves along $H//[001]$ for temperature ranging from 2 K to 20 K, which shows two magnetic steps before saturation below the phase transition temperature. These magnetic steps vanish for those IM(H) curves above the phase transition temperature. Based on these IM(H) curves, the Arrott plot is constructed using critical exponents from the mean-field theory with $\beta = 0.5$ and $\gamma = 1.0$, as shown in Fig. 4(b). The Arrott plot of DyBi does not show a series of parallel lines, indicating that the magnetic interaction in DyBi cannot be described by the conventional Landau mean-field model.

More generally, $M(H)$ curves in the vicinity of a phase transition can be described by the Arrott-Noakes equation of state as follows [25]:

$$(H/M)^{1/\gamma} = (T - T_C)/T_C + (M/M_1)^{1/\beta}, \tag{1}$$

where M_1 is a constant, and β and γ are critical exponents. According to Eq. (1), a plot of $M^{1/\beta}$ vs $(H/M)^{1/\gamma}$, also known as the modified Arrott plot (MAP), should consist of a series of parallel straight lines. Owing to the three-dimensional nature of the crystal structure, three-dimensional theoretical models such as the tricritical mean-field model ($\beta = 0.25, \gamma = 1.0$), 3D-Ising model ($\beta = 0.325, \gamma = 1.240$), 3D-$XY$ model ($\beta = 0.346, \gamma = 1.316$), and 3D-Heisenberg model ($\beta = 0.365, \gamma = 1.386$) are used to construct the MAPs. As shown in Figs. 5(a)–5(d), four groups of possible exponents exhibit nearly straight lines in the high-field region. The normalized slopes (NSs) are fitted out, which are defined as NS $= S(T)/S(T_C)$, where S is the slope of a single line of $M^{1/\beta}$ vs $(H/M)^{1/\gamma}$. By comparing the NS to the ideal value of unity, the best model can be identified. The NSs of various theoretical models are plotted in Fig. 6(a). It can be seen that the tricritical mean-field model deviates the least from 1 among the models considered, indicating that the tricritical mean-field model is the best one to describe magnetic interaction in DyBi.

The magnetic critical exponents β, γ, and δ, in particular, are linked to the spontaneous magnetization (M_S), the inverse initial susceptibility (χ_0^{-1}), and the critical isotherm $M(H)$ at T_C, respectively. In the vicinity of T_C, they satisfy the following equations [26,27]:

$$M_S(T) = M_0(-\varepsilon)^{\beta}, \varepsilon < 0, T < T_C, \tag{2}$$

$$\chi_0^{-1}(T) = (h_0/M_0)\varepsilon^{\gamma}, \varepsilon > 0, T > T_C, \tag{3}$$

$$M = DH^{1/\delta}, \varepsilon = 0, T = T_C, \tag{4}$$

where $\varepsilon = (T - T_C)/T_C$ is the reduced temperature, M_0/h_0, and D are critical amplitudes. Critical exponents β, γ, and δ reveal important information about the nature of spin interaction, spin dimensionality, and magnetic coupling decaying length. Precise β and γ can be obtained by an iteration method [28,29]. Since the tricritical mean-field model best describes DyBi, Fig. 5(a) is used as a starting point for generating the exponents. The spontaneous magnetization [$M_S(T, 0)$] and inverse initial susceptibility [$\chi_0^{-1}(T, 0)$] can be obtained from intercepts of the linear extrapolation from the high-field region to axes $M^{1/\beta}$ and $(H/M)^{1/\gamma}$. By fitting to Eqs. (2) and (3), one obtains a set of β and γ, which are used to reconstruct a new MAP. The linear extrapolation from the high-field region subsequently yields another set of $M_S(T, 0)$ and $\chi_0^{-1}(T, 0)$.

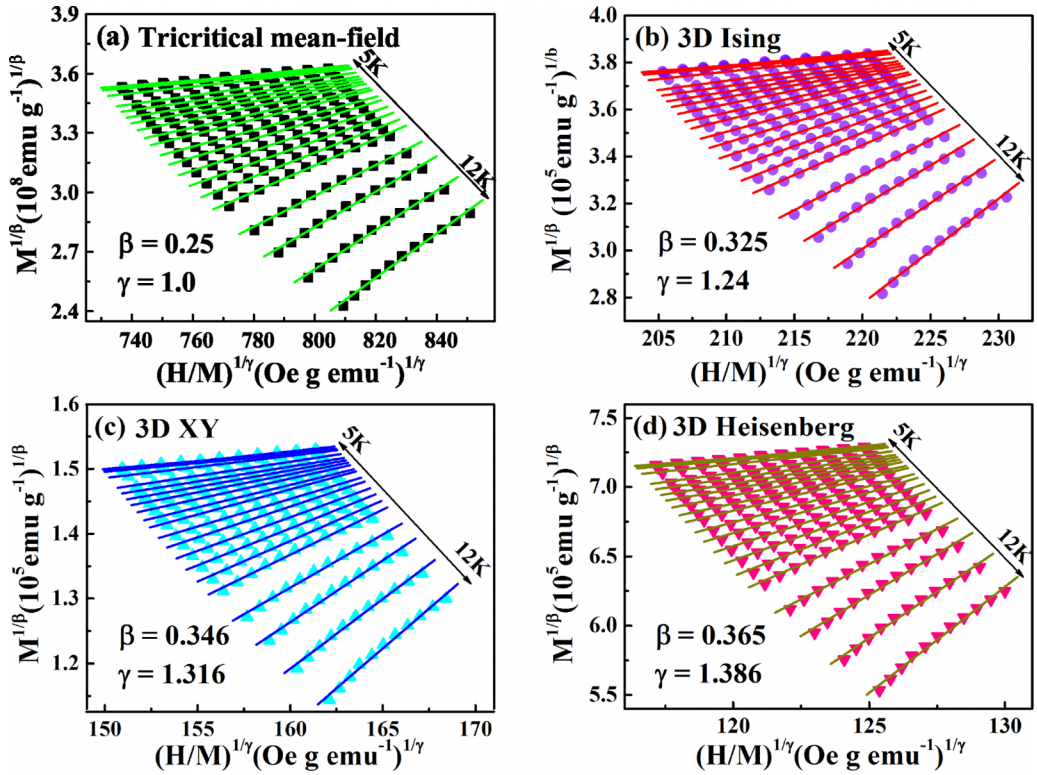

FIG. 5. Modified Arrott plots under different theoretical models: (a) tricritical mean field, (b) 3D Ising, (c) 3D *XY*, (d) 3D Heisenberg.

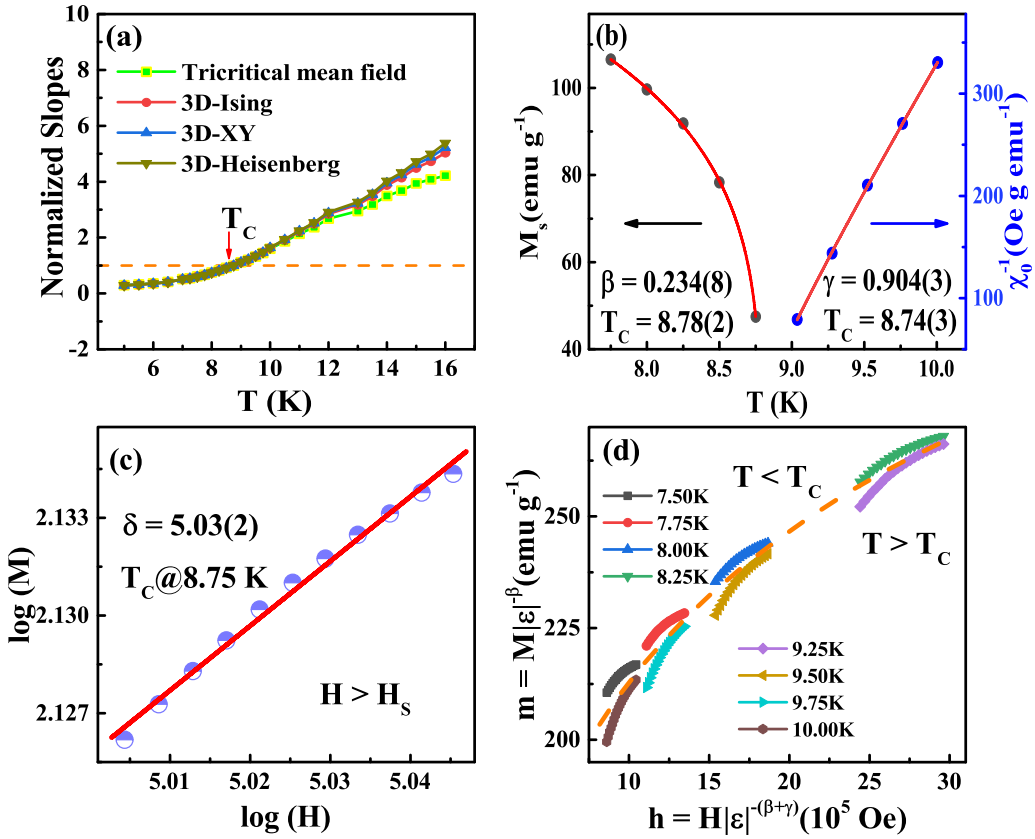

FIG. 6. (a) Temperature dependence of normalized slope [NS(T)] for different theoretical models. (b) Temperature dependence of spontaneous magnetization [$M_S(T)$] and inverse initial susceptibility [$\chi_0^{-1}(T)$] with fitted curves. (c) IM(H) at T_C on log-log scale. (d) Renormalization magnetization vs renormalization field (m vs h).

TABLE I. Critical exponents of DyBi, DySb, and different theoretical models.

Composition	Technique	Reference	T_C	β	γ	δ
DyBi	Experiment	This work	8.75	0.234(8)	0.904(3)	5.03(2)
DySb	Experiment	[32]	7.5	0.244(2)	0.827(2)	4.425(1)
Tricritical mean field	Theory	[35]		0.25	1.0	5.0
3D Ising	Theory	[36]		0.325	1.24	4.82
3D *XY*	Theory	[36]		0.346	1.316	4.81
3D Heisenberg	Theory	[36]		0.365	1.386	4.8
Mean field	Theory	[36]		0.5	1.0	3.0

Thus, another set of β and γ can be obtained. This procedure is repeated until β and γ converge to fixed values. Figure 6(b) depicts the final temperature-dependent $M_S(T)$ and $\chi_0^{-1}(T)$ in the vicinity of the phase transition, which yields $\beta = 0.234(8)$ with $T_C = 8.78(2)$ and $\gamma = 0.904(3)$ with $T_C = 8.74(3)$. Figure 6(c) depicts the IM(H) at the critical temperature $T_C = 8.75$ K on log-log scale. When $H > H_S$, IM(H) at T_C exhibits a straight line on log-log scale. Thus, using Eq. (4), the third critical exponent $\delta = 5.03(2)$ can be determined in the high-field region ($H > H_S$). Furthermore, the exponents can be examined using the Widom scaling relation, which combines β, γ, and δ as follows [30,31]:

$$\delta = 1 + \frac{\gamma}{\beta}. \tag{5}$$

Following Eq. (5) and using the values of β and γ obtained from the MAP analysis, $\delta = 4.851(4)$ was calculated, which is close to the critical isotherm analysis. This indicates the self-consistency and reliability of these obtained critical exponents.

To guarantee the validity of these critical exponents as well as T_C, it is necessary to determine whether they fulfill the magnetic equation of state in the asymptotic critical region, which is given below [27]:

$$M(H, \varepsilon) = \varepsilon^{\beta} f_{\pm}(H/\varepsilon^{\beta+\gamma}). \tag{6}$$

Equation (6) can also be expressed in terms of renormalized magnetization $m \equiv \varepsilon^{-\beta} M(H, \varepsilon)$ and the renormalized field $h \equiv H\varepsilon^{-(\beta+\gamma)}$ as

$$m = f_{\pm}(h), \tag{7}$$

where $f_{\pm}$ are regular functions with f_+ for $T > T_C$ and f_- for $T < T_C$. According to Eq. (7), for the correct choice of critical exponents, m vs h must generate two universal curves above and below T_C [27]. Figure 6(d) depicts m vs h in the high-field region ($H > H_S$), where all data collapse on two independent branches above and below T_C. This clearly shows that the interactions are properly renormalized in a critical regime by following the scaling equation of state. Table I compares the critical exponents of DyBi and DySb, as well as those of theoretical models. The critical exponents of DyBi are mostly close to those of a tricritical mean-field model similar to that of DySb, indicating a tricritical phenomenon. However, the critical exponents of DyBi approach the theoretical prediction more closely than those of DySb. The deviation of the critical exponents from the theoretical model is generally caused by the multiple and complex magnetic interactions in a real system. It is noted that the AFM interaction in DyBi is stronger than that in DySb, which will suppress other interactions to allow one single magnetic interaction to dominate the system. The single dominant interaction makes DyBi approach more closely to the ideal theoretical model. In general, a tricritical phenomenon occurs in a system with multiple phases that are induced by pressure, field, doping, etc. [32,33]. A tricritical point (TCP) appears when three phases converge at the same point on the phase diagram. Therefore, constructing a phase diagram is critical for comprehending the various phases in DyBi.

Figure 7 depicts the final MAPs with experimentally obtained critical exponents $\beta = 0.234$ and $\gamma = 0.904$. In the high-field region, the MAP of $M^{1/\beta}$ vs $(H/M)^{1/\gamma}$ exhibits a series of straight lines, as shown in Fig. 7(a). Instead, the magnified MAP of $M^{1/\beta}$ vs $(H/M)^{1/\gamma}$ in the low-field region exhibits complex behaviors due to the field-induced phase transitions, as shown in Fig. 7(b). Several inflection points corresponding to the field-induced phase transitions can be found in the MAP in Fig. 7(b), which supplies a method to generate an H-T phase diagram [32,33]. Divergence on the phase boundary is caused by the change in magnetic interactions, which results in an inflection point on MAP [29,33,34]. Extracting these inflection points from Fig. 7(b), a detailed H-T phase diagram can be constructed. Figure 8(a) depicts the detailed H-T phase diagram for single-crystal DyBi with $H//[001]$. Similarly, detailed H-T phase diagrams for $H//[011]$ and $H//[111]$ are also constructed, as shown in Figs. 8(b) and 8(c). DyBi and its isostructural solids, such as DySb, are demonstrated to exhibit simultaneous structural and magnetic transitions [19,32]. These compounds usually undergo magnetic transitions at low temperatures. At the same time, their crystal structure evolves into a tetragonal or pseudotetragonal one accompanied by a shrinkage of c axis [19,32]. The low-temperature specific heat of DyBi exhibits a sharp peak and a decline in magnetic entropy at the phase transition temperature, suggesting a first-order phase transition and a magnetic ordering [23]. Temperature-dependent resistivity in isostructural CeBi shows an abnormal peak near T_N, and large negative MR is observed near the critical fields in isothermal $R(H)$ curves, indicating magnetoelectronic coupling in this system [37]. Dysprosium (Dy) monopnictides provide a variety of magnetic ground states because the exchange parameter in these systems changes from negative to positive depending on the size of lattice constant a (that varies with the choice of *Pn* element). Replacing the *Pn* in *RPn* from N to Bi, the magnetic ground state changes from FM (DyN) to ferrimagnetic (FIM) (DyP and DyAs) to AFM (DySb and DyBi) states. In an AFM ground state, the neutron diffraction

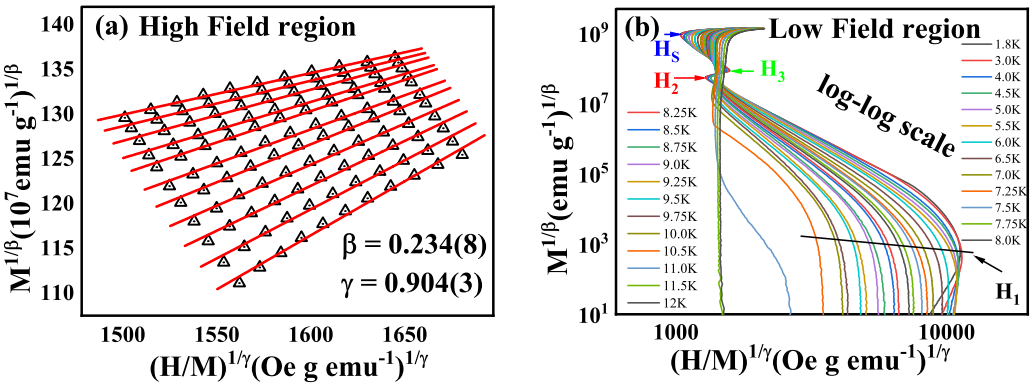

FIG. 7. Modified Arrott plots (MAPs) with the obtained critical exponents: (a) MAP in the high-field region; (b) that in the low-field region.

revealed that magnetic moments (Dy^{3+} ions) are typically aligned in type-II AFM structure, i.e., NiO-type AFM state [20,24,38]. In this magnetic structure, opposite FM (111) planes alternatively stack along the [111] direction (here [111] refers to the tetragonal space group), as illustrated in Fig. 8(d). Such an AFM ground state can be transformed to an FM state by applying an external magnetic field through an intermediate phase [19]. Due to the anisotropic magnetic behaviors, the applied magnetic field realizes different magnetic phase transitions and states along different crystal orientations.

For single-crystal DyBi with $H//[001]$, the magnetization curve exhibits four inflection points marked as H_1, H_2, H_3, and H_S. The phase below H_1 is unambiguously attributed to the ground state, which has been determined to be the NiO-type AFM state by the neutron diffraction [20]. The NiO-type AFM ground state of DyBi is manifested as opposite FM (111) planes alternatively stacked along the [111] direction [20,38]. Based on magnetic moment calculations, Hulliger *et al.* proposed that the NiO-type AFM ground state can be modulated to an intermediate phase and then to the FM phase via external magnetic field [24], as shown in Figs. 8(e) and 8(f). Furthermore, they predicted that the critical field of DyBi for $H//[011]$ and $H//[111]$ would be very large due to the large anisotropy energy [24]. In this intermediate phase called HoP-type AFM state schematically shown in Fig. 8(e), the moments in one of the two nearest (011) planes are rotated 90° to the [110] direction, and hence the magnetization along [001] suddenly increases to half of its saturation value [24]. Therefore, H_2 is a signal of the field-modulated HoP-type AFM phase. However, the transformation of magnetic structure from NiO-type to HoP-type is not abrupt. Magnetic torque is induced in NiO-type structure that transforms the magnetic structure gradually into HoP-type AFM with increasing magnetic field. Thus, a mixed phase (coexistence I between H_1 and H_2) exists between NiO- and HoP-type AFM structures. At higher fields, the HoP-type AFM transforms to another coexistence II, and then eventually into the forced ferromagnetic (FFM) phase. The FFM phase becomes dominant in the higher-field region (above H_S), where the M_S is close to the theoretical saturation moment of Dy^{3+}. Thus, the coexistence II between H_3 and H_S is a mix phase of HoP-type AFM and FFM. In addition, the transition from AFM to PM is first order while the transition from PM to FFM is second order demonstrated by the $M(T)$ curves in Fig. 2. These three phases converge at one point on the phase diagram, which is determined as TCP. The presence of a TCP is consistent with

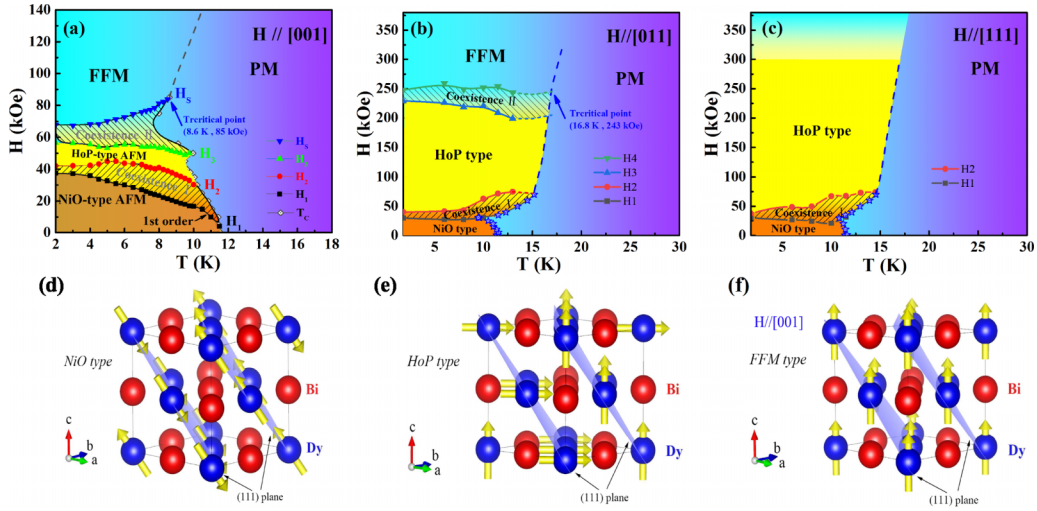

FIG. 8. *H-T* phase diagrams for single-crystal DyBi with (a) $H//[001]$, (b) $H//[011]$, and (c) $H//[111]$. Magnetic structures of (d) NiO-type AFM, (e) HoP-type AFM, and (f) FFM.

the tricritical phenomenon for DyBi, which exhibits multiple phases. In the phase diagram, the TCP (8.6 K, 85 kOe) is determined for $H//[001]$ at the intersection of AFM, PM, and FFM states. For $H//[011]$ and $H//[111]$ as shown in Figs. 8(b) and 8(c), this spin flip from NiO-type AFM to the HoP-type one occurs at slightly lower fields (∼30 kOe). However, the spin flip from HoP-type AFM to FFM occurs at much higher field. The spin flip occurs at 240 kOe (24 T) for $H//[011]$, while it is not observed up to 32 T for $H//[111]$. The TCP for $H//[011]$ is estimated as (16.8 K, 243 kOe), while that for $H//[111]$ is beyond the experimental measurement range. The magnetic behaviors of DyBi are similar to those of DySb, but more complex. In the phase diagram, the AFM regions are larger, and T_C is higher, indicating stronger AFM interaction in DyBi. The magnetization step at 24 T, in particular, had never been reported.

The extremely large critical fields for $H//[011]$ and $H//[111]$ indicate high anisotropy energies in DyBi. The spin Hamiltonian of the ground state in the presence of an external magnetic field can be written as

$$\begin{aligned} H_{\text{spin}} &= H_{\text{inner}} + H_{\text{inter}} + H_A + H_{\text{field}} \\ &= -\sum_{\langle ij\rangle} J^{//} S_i \cdot S_j + \sum_{\langle ij\rangle} J^{\perp} S_i \cdot S_j \\ &\quad + \sum_{\langle i\rangle} \left(\alpha^{[001]} S_i^{[001]} + \alpha^{[011]} S_i^{[011]} + \alpha^{[111]} S_i^{[111]}\right) \\ &\quad + \sum_{\langle i\rangle} \mathbf{H} \cdot \mathbf{S}_i, \end{aligned} \tag{8}$$

where H_{inner}, H_{inter}, H_A, and H_{field} represent the inner-spin-coupling, the inter-spin-coupling, the magnetic anisotropy, and external field Hamiltonian, respectively. H_{inner} corresponds to the in-plane FM interaction within the (111) plane, while H_{inter} corresponds to the out-of-plane AFM one perpendicular to the (111) plane. The αS_i represents the magnetic anisotropy (α is magnetic anisotropy coefficient), where $\alpha^{[111]} > \alpha^{[011]} > \alpha^{[001]}$. The system maintains a NiO-type AFM phase in the ground state ($H_{\text{field}} = 0$). When the field strength increases, the energy of H_{field} increases, resulting in the formation of the HoP-type AFM state. As the energy of H_{field} further increases, the HoP-type AFM state is eventually polarized to the FFM state. Considering the energy of exchange interaction $\Delta E = \mu H$ (where μ is the effective magnetic moment, and $\mu \sim 9\ \mu_B$ at 24 T for $H//[011]$), it can be obtained that $\Delta E_{[011]} \approx 12.51$ meV. On the other hand, taking account of $\Delta E \propto \Delta M$ [ΔM is magnetization change at the magnetic phase transition, $\Delta M_{[011]} \sim 1\ \mu_B$ and $\Delta M_{[111]} \sim 3\ \mu_B$ as shown in Fig. 3(a)], the critical field for $H//[111]$ can be obtained as $H_{[111]} = \frac{\mu_{[011]}\Delta M_{[111]}}{\mu_{[111]}\Delta M_{[011]}} H_{[011]}$ (where $\mu_{[011]} \sim 9\ \mu_B$, $\mu_{[111]} \sim 7\ \mu_B$, and $H_{[011]} = 24$ T). The critical field $H_{[111]}$ for $H//[111]$ is estimated to be as high as 92 T. A thorough investigation on the magnetization of DyBi, a typical material in this family, is required to uncover and clarify the exotic magnetism in this system.

IV. CONCLUSION

We perform a systematical investigation on multiple phases and magnetic interactions in the rare-earth monopnictide DyBi. A magnetic field up to 32 T is applied along [001], [011], and [111], which reveals anisotropic magnetization as well as distinct field-induced metamagnetic transitions in single-crystal DyBi. The critical behavior analysis for $H//[001]$, a direction with typical magnetism and transitions, yields critical exponents $\beta = 0.234(8)$, $\gamma = 0.904(3)$, and $\delta = 5.03(2)$. The obtained critical exponents are consistent with the theoretical prediction of a tricritical mean-field model, indicating a tricritical phenomenon with multiple phases. The H-T phase diagrams for $H//[001]$, $H//[011]$, and $H//[111]$ are constructed, which unveil multiple magnetic structures such as the NiO-type AFM ground state, the field-induced HoP-type AFM, and the FFM phases. TCPs are determined at the intersections of the AFM, FFM, and PM phases, with TCP = (8.6 K, 85 kOe) for $H//[001]$ and (16.8 K, 243 kOe) for $H//[011]$. The recognition of multiple phases implies delicate competition and balance between variable interactions and couplings, laying a solid foundation for understanding critical phenomena in this system.

ACKNOWLEDGMENTS

The authors thank Prof. N. Hao for beneficial discussion. This work was supported by the National Key R&D Program of China (Grant No. 2017YFA0303201), the National Natural Science Foundation of China (Grants No. 12074386, No. 11874358, No. 11874158, No. U1732276, and No. 12204006), the Alliance of International Science Organizations (Grant No. ANSO-VF-2021-03), the Collaborative Innovation Program of Hefei Science Center, CAS (Grant No. 2021HSC-CIP006), Anhui Provincial Natural Science Foundation (Grant No. 2108085QA21), and the Key Project of Natural Scientific Research of Universities in Anhui Province (Grant No. K120462009). A portion of this work was supported by the High Magnetic Field Laboratory of Anhui Province.

[1] L. Petit, Z. Szotek, M. Lüders, and A. Svane, J. Phys.: Condens. Matter **28**, 223001 (2016).

[2] L. K. Zeng, R. Lou, D. S. Wu, Q. N. Xu, P. J. Guo, L. Y. Kong, Y. G. Zhong, J. Z. Ma, B.-B. Fu, P. Richard, P. Wang, G. T. Liu, L. Lu, Y.-B. Huang, C. Fang, S.-S. Sun, Q. Wang, L. Wang, Y.-G. Shi, H. M. Weng *et al.*, Phys. Rev. Lett. **117**, 127204 (2016).

[3] X. H. Niu, D. F. Xu, Y. H. Bai, Q. Song, X. P. Shen, B. P. Xie, Z. Sun, Y. B. Huang, D. C. Peets, and D. L. Feng, Phys. Rev. B **94**, 165163 (2016).

[4] P.-J. Guo, H.-C. Yang, B.-J. Zhang, K. Liu, and Z.-Y. Lu, Phys. Rev. B **93**, 235142 (2016).
[5] N. Wakeham, E. D. Bauer, M. Neupane, and F. Ronning, Phys. Rev. B **93**, 205152 (2016).
[6] F. Wu, C. Y. Guo, M. Smidman, J. L. Zhang, and H. Q. Yuan, Phys. Rev. B **96**, 125122 (2017).
[7] Y. Wu, Y. Lee, T. Kong, D. Mou, R. Jiang, L. Huang, S. L. Bud'ko, P. C. Canfield, and A. Kaminski, Phys. Rev. B **96**, 035134 (2017).
[8] M. N. Ali, J. Xiong, S. Flynn, J. Tao, Q. D. Gibson, L. M. Schoop, T. Liang, N. Haldolaarachchige, M. Hirschberger, N. P. Ong, and R. J. Cava, Nature (London) **514**, 205 (2014).
[9] J. Feng, Y. Pang, D. Wu, Z. Wang, H. Weng, J. Li, X. Dai, Z. Fang, Y. Shi, and L. Lu, Phys. Rev. B **92**, 081306(R) (2015).
[10] T. Liang, Q. Gibson, M. N. Ali, M. Liu, R. J. Cava, and N. P. Ong, Nat. Mater. **14**, 280 (2015).
[11] X. Huang, L. Zhao, Y. Long, P. Wang, D. Chen, Z. Yang, H. Liang, M. Xue, H. Weng, Z. Fang, X. Dai, and G. Chen, Phys. Rev. X **5**, 031023 (2015).
[12] C. Shekhar, A. K. Nayak, Y. Sun, M. Schmidt, M. Nicklas, I. Leermakers, U. Zeitler, Y. Skourski, J. Wosnitza, Z. Liu, Y. Chen, W. Schnelle, H. Borrmann, Y. Grin, C. Felser, and B. Yan, Nat. Phys. **11**, 645 (2015).
[13] M. Zeng, C. Fang, G. Chang, Y.-A. Chen, T. Hsieh, A. Bansil, H. Lin, and L. Fu, arXiv:1504.03492.
[14] J. Nayak, S.-C. Wu, N. Kumar, C. Shekhar, S. Singh, J. Fink, E. E. D. Rienks, G. H. Fecher, S. S. P. Parkin, B. Yan, and C. Felser, Nat. Commun. **8**, 13942 (2017).
[15] Z. M. Wu, Y. R. Ruan, F. Tang, L. Zhang, Y. Fang, J.-M. Zhang, Z. D. Han, R. J. Tang, B. Qian, and X. F. Jiang, New J. Phys. **21**, 093063 (2019).
[16] C. Guo, C. Cao, M. Smidman, F. Wu, Y. Zhang, F. Steglich, F.-C. Zhang, and H. Yuan, npj Quantum Mater. **2**, 39 (2017).
[17] C.-G. Duan, R. F. Sabirianov, W. N. Mei, P. A. Dowben, and S. S. J. E. Y. Tsymbal, J. Phys.: Condens. Matter **19**, 315220 (2007).
[18] C. E. Matt, Y. Liu, H. Pirie, N. C. Drucker, N. H. Jo, B. Kuthanazhi, Z. Huang, C. Lane, J.-X. Zhu, P. C. Canfield, and J. E. Hoffman, Phys. Rev. B **105**, 085134 (2022).
[19] F. Hulliger, J. Magn. Magn. Mater. **15-18**, 1243 (1980).
[20] N. Nereson and G. Arnold, J. Appl. Phys. **42**, 1625 (1971).
[21] D. C. Gupta and I. H. Bhat, J. Mol. Model. **19**, 5343 (2013).
[22] K. Yoshihara, J. B. Taylor, L. D. Calvert, and J. G. Despault, J. Less-Common Met. **41**, 329 (1975).
[23] H. Wada, H. Imai, and M. Shiga, J. Alloys Compd. **218**, 73 (1995).
[24] E. Bucher, R. J. Birgeneau, J. P. Maita, G. P. Felcher, and T. O. Brun, Phys. Rev. Lett. **28**, 746 (1972).
[25] A. Arrott and J. E. Noakes, Phys. Rev. Lett. **19**, 786 (1967).
[26] M. E. Fisher, Rep. Prog. Phys. **31**, 418 (1968).
[27] N. D. Mermin, Science **176**, 502 (1972).
[28] H. C. Chauhan, B. Kumar, A. Tiwari, J. K. Tiwari, and S. Ghosh, Phys. Rev. Lett. **128**, 015703 (2022).
[29] H. Han, W. Liu, Y. Dai, Y. Gao, Z. Tian, J. Fan, S. Zhou, L. Pi, C. Zhang, L. Zhang, and Y. Zhang, Phys. Rev. B **98**, 054403 (2018).
[30] L. P. Kadanoff, Phys. Phys. Fiz. **2**, 263 (1966).
[31] B. Widom, J. Chem. Phys. **43**, 3898 (1965).
[32] W. Liu, D. Liang, F. Meng, J. Zhao, W. Zhu, J. Fan, L. Pi, C. Zhang, L. Zhang, and Y. Zhang, Phys. Rev. B **102**, 174417 (2020).
[33] L. Zhang, D. Menzel, C. Jin, H. Du, M. Ge, C. Zhang, L. Pi, M. Tian, and Y. Zhang, Phys. Rev. B **91**, 024403 (2015).
[34] H. Han, L. Zhang, D. Sapkota, N. Hao, L. Ling, H. Du, L. Pi, C. Zhang, D. G. Mandrus, and Y. Zhang, Phys. Rev. B **96**, 094439 (2017).
[35] K. Huang, *Statistical Mechanics*, 2nd ed. (Wiley, 1987), p. 017202.
[36] S. N. Kaul, J. Magn. Magn. Mater. **53**, 5 (1985).
[37] Y.-Y. Lyu, F. Han, Z.-L. Xiao, J. Xu, Y.-L. Wang, H.-B. Wang, J.-K. Bao, D. Y. Chung, M. Li, I. Martin, U. Welp, M. G. Kanatzidis, and W.-K. Kwok, Phys. Rev. B **100**, 180407(R) (2019).
[38] K. Arai, T. Okuda, A. Tanaka, M. Kotsugi, K. Fukumoto, T. Ohkochi, T. Nakamura, T. Matsushita, T. Muro, M. Oura, Y. Senba, H. Ohashi, A. Kakizaki, C. Mitsumata, and T. Kinoshita, Phys. Rev. B **85**, 104418 (2012).